48th AIAA Aerospace Sciences Meeting Including the New Horizons Forum and Aerospace Exposition
4 - 7 January 2010, Orlando, Florida
AIAA 2010-920

A Comparison of Detached-Eddy Simulation and Reynolds-Stress Modelling Applied to the Flow over a Backward-Facing Step and an Airfoil at Stall

Axel Probst,* Rolf Radespiel,†
Institute of Fluid Mechanics, University of Braunschweig, 38106 Braunschweig, Germany
Christoph Wolf‡, Tobias Knopp§ and Dieter Schwamborn¶
Institute of Aerodynamics and Flow Technology, DLR, 37073 Goettingen, Germany

Flow simulations with the DLR-TAU code of a backward-facing step and an airfoil at stall using two recent versions of detached-eddy simulation (DES), i.e. the delayed DES (DDES) and the improved delayed DES (IDDES), are compared to experiments and RANS computations with the ε^h-Reynolds-stress model (RSM). For the massive separation behind the backward-facing step, both DES variants agree well with measured skin friction and velocity profiles, if a sufficiently fine mesh is applied. The near-wall ε^h-RSM on the other hand overpredicts the separation length. For the stall of the HGR-01 airfoil, which is governed by gradually growing trailing-edge separations, the DES computations suffer from poor predictions of the developing boundary layer, issues with modelled-stress depletion and a delayed onset of resolved turbulence in the LES region. Overall, the application of DDES and IDDES to airfoil stall is considered unsuccessful in this study as even beyond maximum lift no turbulence is resolved in the separated region. For this flow, the ε^h-RSM compares much better to PIV data and static pressure measurements.

Nomenclature

c	Chord length
c_f	Skin friction coefficient
c_l	Lift coefficient
c_p	Pressure coefficient
$C_{\mathrm{DES}} = 0.65$	DES constant
d_w	Wall distance
f_d, f_{dt}	Delay functions
h	Step height
h_{max}	Maximum grid spacing
h_{wn}	Wall-normal grid spacing
k	Turbulent kinetic energy
l	Length scale
L_z	Spanwise grid extent
n_z	Spanwise layer number
Q	Q-criterion
Re	Reynolds number
Re_t	Turbulent Reynolds number
$S_{\varepsilon 4}$	Pressure gradient term
S_l	Length scale limiting term
$\widetilde{S}$	Spalart-Allmaras vorticity
$U_i = U, V, W$	Velocity components
U_∞	Freestream velocity
$u_i = u, v, w$	Turbulent fluctuation velocities
$\overline{u_i u_j}$	Reynolds-stress tensor
y_n	Wall-normal coordinate
Symbols:	
α	Angle of attack
Δ	Subgrid length-scale
$\Delta x, \Delta y, \Delta z$	Grid spacing
ε	Dissipation rate of turbulent energy
ε^h	Homogeneous part of ε
$\tilde{\varepsilon}^h$	Isotropic part of ε^h
ε_{ij}	Dissipation rate tensor
$\kappa = 0.41$	von Kármán constant
ν	Kinematic viscosity
ν_t	Kinematic eddy viscosity
$\tilde{\nu}$	Spalart-Allmaras viscosity
Ψ	Low-Reynolds correction term

*Research scientist, AIAA Member.
†Professor, AIAA Senior Member.
‡Research scientist.
§Research scientist.
¶Head of C²A²S²E.

I. Introduction

The detailed knowledge of the aerodynamic behaviour of airfoils and wings at stall conditions is of major importance in airplane design, but it still suffers from the difficulties to accurately compute the onset and the development of flow separations at high angles of attack. While conventional turbulence models on the RANS und URANS level often fail to capture the effects of strong pressure gradients, streamline curvature and the unsteadiness associated with separated flow,[1] the application of large-eddy simulation (LES)[2] to directly resolve the relevant turbulent structures is severely limited by the high computational costs at flight Reynolds numbers.[3]

For this reason, attention has been drawn on hybrid RANS/LES approaches which try to combine the superior accuracy of LES in separated flow regions with the efficiency of RANS modelling in attached boundary layers. The required distinction between the RANS and the LES regions can either be fixed by the user (zonal approach),[4] or it can be the outcome of the hybrid RANS/LES model's formulation itself (non-zonal approach). As the onset and the size of the pressure-induced separations on airfoils and wings are usually not known a priori and, in addition, vary strongly with the angle of attack, non-zonal approaches are considered better suited for simulating the complex stall process.

The most popular non-zonal RANS/LES hybrid has been the detached-eddy simulation[3] which applies the Spalart-Allmaras model[5] in the RANS region and determines the RANS and LES branches purely based on grid properties. However, if the grid does not fulfil certain criteria, the RANS/LES interface in DES may come to lie too deep within the (attached) boundary layer, leading to a unphysical reduction of the modelled Reynolds stresses and, in the worst case, to so-called grid-induced separations.[6] To combat this grid-dependency, a "shielding" mechanism has been introduced in a new DES version called Delayed DES (DDES)[6] in order to prevent the boundary layer from separating prematurely. Another recent step was the extension of DDES by wall-modelled LES capabilities[7] which led to the Improved DDES (IDDES).[8]

Both these new DES methods have been successfully applied to massively separated flow, sometimes fixed by a sudden change in the geometry, as well as to cases with only mild separation which are so small that usually the pure RANS solution is returned.[9,10] However, this paper focuses on the whole process of airfoil stall, covering the range of almost fully attached flow up to clearly beyond maximum lift, where pressure-induced trailing-edge separations cover large parts of the airfoil's upper surface.

After a brief description of the numerical models, a computational study of the backward-facing step flow by Driver and Seegmiller[11] is presented to validate the implementation of DDES and IDDES in the flow solver DLR-TAU.[12] The new DES models are then applied to the well-documented stall process of the tail-plane airfoil HGR-01 at Re = 0.65 Mio.[13] The results are compared to detailed measurements including PIV as well as to advanced RANS simulations with the Low-Re ε^h-Reynolds-stress model (RSM),[14] which was found to yield good results for airfoil stall in previous studies.[15]

II. Numerical method

The simulations presented in this paper are performed with the DLR-TAU code[12] which is a finite-volume flow solver for unstructured and hybrid meshes. To ensure low numerical diffusion all DES computations employ second-order central discretization with matrix-based artificial dissipation and low-Mach number preconditioning, while time integration is based on a second-order implicit dual-timestepping scheme. The approaches to treat turbulence in this work are described in the following sections.

II.A. Detached-Eddy Simulation (DES)

Detached-eddy simulation (DES)[3] is a non-zonal hybrid RANS-LES model that can be based on all common RANS models. DES is obtained by replacing the original turbulent length scale in the dissipation term of the underlying RANS-model (which is the one-equation Spalart-Allmaras (SA) model[5] in this publication) by a new length scale l_{DES}, resulting in an LES-like behaviour away from the wall. To be more precise, the production and destruction terms $P_{\tilde{\nu}}$ and $D_{\tilde{\nu}}$ in the SA-RANS model are:

$$P_{\tilde{\nu}} = c_{b1}\widetilde{S}\tilde{\nu}, \quad D_{\tilde{\nu}} = c_{w1} f_w \left(\frac{\tilde{\nu}}{d_w}\right)^2 \quad . \tag{1}$$

Here $\tilde{\nu}$ is the Spalart-Allmaras viscosity, $\widetilde{S}$ is a modified vorticity, f_w is a model functions and c_{b1} and c_{w1} are constants. The turbulent length scale in the destruction term $D_{\tilde{\nu}}$, which is given by the wall distance d_w in Eq. (1), is then replaced by:

$$l_{\text{DES}} = \min(d_w, C_{\text{DES}}\Delta), \quad \Delta = h_{max} = \max[\Delta x, \Delta y, \Delta z], \quad C_{\text{DES}} = 0.65 \quad . \tag{2}$$

Near a wall l_{DES} equals d_w, ensuring normal SA-RANS mode. Farther away from a wall $l_{\text{DES}} = C_{\text{DES}}\Delta$, leading to

$$\tilde{\nu} \sim \tilde{S}\Delta^2 \tag{3}$$

which is analogous to a LES-Smagorinsky model.

II.B. Delayed Detached-Eddy Simulation (DDES)

As a potential shortcoming in the DES model described above, the filter Δ is only based on grid properties, but not on the actual flow field. If a fine grid is used, the LES region of the DES model can be shifted into the boundary layer. This may lead to grid-induced separation resulting from modelled-stress depletion, which is especially undesirable when dealing with airfoil stall. Moreover, grid-dependent flow solutions can occur, making a grid convergence study virtually impossible.

In order to address these issues, the Delayed DES (DDES) has been introduced.[6] Here the RANS-LES switch is also based on local flow properties, thereby eliminating most disadvantages of the original DES model. The length scale l_{DDES} in DDES is given by:

$$l_{\text{DDES}} = d_w - f_d \cdot max(0, d_w - \ \Psi C_{\text{DES}}\Delta), \quad f_d = 1 - \tanh\left[(8r_d)^3\right], \quad r_d = \frac{\nu + \nu_t}{\sqrt{U_{i,j}U_{i,j}}\kappa^2 d_w^2} \quad . \tag{4}$$

Here ν is the molecular viscosity, ν_t is the kinematic eddy viscosity, $U_{i,j}$ are the velocity gradients and $\kappa = 0.41$ is the von Kármán constant. Within a boundary layer $f_d \equiv 0$, leading to $l_{\text{DDES}} = d_w$ and hereby ensuring normal SA-RANS-mode. Outside the boundary layer $f_d \equiv 1$, resulting in $l_{\text{DDES}} = min(d_w,\ \Psi C_{\text{DES}}\Delta)$, which is the original DES model introduced in II.A.

The term Ψ in Eq. (4) is a low-Reynolds correction[6] required to obtain Smagorinsky-like behaviour in the LES branch at locally low eddy-viscosity levels:

$$\Psi^2 = \frac{1 - c_{b1} f_{v2} / (c_{w1}\kappa^2 f_w^\star)}{f_{v1}} \quad . \tag{5}$$

Here f_{v1}, f_{v2}, and $f_w^\star$ are functions and constants from the SA-RANS model. The original formulation in Spalart et al.[6] includes another parameter f_{t2} that accounts for laminar-turbulent transition in the SA model. As in the examples considered here transition only occurs in the RANS region and as the activation of the turbulence model is treated differently in the DLR-TAU Code, this term is neglected.

II.C. Improved Delayed Detached-Eddy Simulation (IDDES)

Besides classical applications of the detached-eddy simulation, where the LES region is usually strictly limited to separated flow, a DES can in principle also act as a wall-modelled LES (WMLES). Here, the large outer part of an attached boundary layer is treated in LES mode, whereas only a thin near-wall region is modelled via RANS. However, it was found that in both DES and DDES, the modelled and the resolved parts of the logarithmic layer are mismatched and lead to wrong skin friction predictions. This defect has been addressed with a new version called Improved DDES (IDDES).[8]

The first key element in IDDES is a redefinition of the subgrid length-scale, since the classical length-scale Δ in Eq. (2) was found to require different subgrid-model constants when applied to wall-bounded turbulence and free turbulent flow, respectively. Therefore, suited length-scale definitions for the two limiting cases are derived to construct a linear blending which satisfies both demands in a single subgrid length-scale:

$$\Delta_{\text{IDDES}} = \min\left\{\max\left[C_w d_w, C_w h_{\max}, h_{wn}\right], h_{\max}\right\} \quad . \tag{6}$$

It involves the wall distance d_w, the wall-normal grid spacing h_{wn} and an empirical constant $C_w = 0.15$.

The second element is the definition of a new hybrid length-scale l_{hyb} to be inserted in the turbulence model's destruction term instead of the DDES length-scale l_{DDES} from Eq. (4). It acts much like DDES in unresolved, attached boundary layers (RANS mode) and free turbulent flow (LES mode), respectively, but quite differently in boundary layers containing resolved turbulence (WMLES mode) in order to avoid the log-layer mismatch. For this purpose, two empirical functions, f_B and f_e, are introduced to properly control the blending between the RANS length-scale $l_{\mathrm{RANS}} = d_w$ for the SA model and the LES scale $l_{\mathrm{LES}} = \Psi C_{\mathrm{DES}} \Delta_{\mathrm{IDDES}}$ in the WMLES branch as:

$$l_{\mathrm{WMLES}} = f_B \left(1 + f_e\right) l_{\mathrm{RANS}} + \left(1 - f_B\right) l_{\mathrm{LES}} \quad . \tag{7}$$

Here, f_B is to provide a more rapid switching from RANS to LES mode with increasing wall distance

$$f_B = \min\left\{2\exp\left(-9\alpha^2\right), 1\right\} \quad , \quad \alpha = 0.25 - d_w/h_{\max} \quad , \tag{8}$$

whereas the “elevating-function” f_e locally increases the modelled Reynolds stresses near the RANS-LES interface to correct the log-layer mismatch:

$$f_e = \max\left\{\left(f_{e1} - 1\right), 0\right\} \Psi f_{e2} \quad . \tag{9}$$

This function includes the low-Reynolds correction term Ψ from Eq. (5) to ensure consistent behaviour of f_e at very low modelled turbulence levels. The functions f_{e1} and f_{e2} read:

$$f_{e1} = \left\{ \begin{array}{cc} 2\exp\left(-11.09\alpha^2\right) & , \quad \alpha \geq 0 \\ 2\exp\left(-9\alpha^2\right) & , \quad \alpha < 0 \end{array} \right\} \quad \text{and} \quad f_{e2} = 1 - \max\left(f_t, f_l\right) \quad . \tag{10}$$

While f_{e1} serves to guide the elevation of the modelled stresses only based on grid properties, the function f_{e2} contains flow field information divided in turbulent (f_t) and laminar (f_l) parts as:

$$f_t = \tanh\left[\left(c_t^2 r_{dt}\right)^3\right] \quad \text{with} \quad r_{dt} = \frac{\nu_t}{\kappa^2 d_w^2 \max\left\{\sqrt{U_{i,j}U_{i,j}}, 10^{-10}\right\}} \quad , \tag{11}$$

$$f_l = \tanh\left[\left(c_l^2 r_{dl}\right)^3\right] \quad \text{with} \quad r_{dl} = \frac{\nu}{\kappa^2 d_w^2 \max\left\{\sqrt{U_{i,j}U_{i,j}}, 10^{-10}\right\}} \quad . \tag{12}$$

It ensures, that the elevation of modelled Reynolds stresses is limited to the case, where the IDDES operates in WMLES mode. The empirical constants are $c_t = 1.63$ and $c_l = 3.55$ for Spalart-Allmaras as the RANS background model.
The remaining blending of the WMLES length-scale, Eq. (7), with the DDES length-scale, Eq. (4), can be written as

$$l_{\mathrm{hyb}} = \tilde{f}_d \left(1 + f_e\right) l_{\mathrm{RANS}} + \left(1 - \tilde{f}_d\right) l_{\mathrm{LES}} \quad . \tag{13}$$

Here, $\tilde{f}_d$ is a blending function

$$\tilde{f}_d = \max\left\{\left(1 - f_{dt}\right), f_B\right\} \quad , \tag{14}$$

with $f_{dt} = 1 - \tanh\left[\left(8 r_{dt}\right)^3\right]$, which is the turbulent part of the DDES delay function f_d, Eq. (4).

II.D. The Near-Wall ε^h-Reynolds-Stress Model

The ε^h-Reynolds-stress model[14] is a RANS model which specifically accounts for near-wall and non-equilibrium turbulence effects. It is based on the Reynolds-stress equations, reading in incompressible form:

$$\frac{D\overline{u_i u_j}}{Dt} = P_{ij} + \Phi_{ij} - \varepsilon_{ij} + D_{ij}^{\nu} + D_{ij}^{t} \quad . \tag{15}$$

Only production P_{ij} and viscous diffusion D_{ij}^{ν} can be computed exactly, whereas the pressure-strain correlation Φ_{ij}, the dissipation rate tensor ε_{ij} and the turbulent diffusion D_{ij}^{t} require modelling approximations. The ε^h-RSM employs a linear pressure-strain correlation including the wall-reflection terms Φ_{ij}^{w}:[16]

$$\Phi_{ij} = -C_1 \varepsilon a_{ij} - C_2 \left(P_{ij} - \frac{2}{3} P_k \delta_{ij}\right) + \Phi_{ij}^{w} \quad \text{with} \tag{16}$$

$$C_1 = C + \sqrt{A} E^2 \ , \ C_2 = 0.8 A^{1/2} \ , \ C = 2.5 A F^{1/4} f \ , \ F = \min\left(0.6; A_2\right) \ , \ f = \min\left[\left(\mathrm{Re}_t/150\right)^{3/2}; 1\right] \ . \tag{17}$$

The near-wall damping functions in Eq. (17) are calibrated based on DNS data and comprise the turbulence Reynolds number Re_t as well as anisotropy invariants of Reynolds stresses (A, A_2) and dissipation rates (E). The length-scale equation is written in terms of the homogeneous part ε^h instead of the commonly used total dissipation rate $\varepsilon = \varepsilon^h + 1/2 \cdot D^\nu$, as this allows for capturing the correct dissipation rate profile near walls:

$$\frac{D\varepsilon^h}{Dt} = -C_{\varepsilon_1}\frac{\varepsilon^h}{k}\overline{u_i u_j}\frac{\partial U_i}{\partial x_j} - C_{\varepsilon_2} f_\varepsilon \frac{\varepsilon^h \tilde{\varepsilon}^h}{k} + C_{\varepsilon_3}\nu\frac{k}{\varepsilon^h}\overline{u_j u_k}\frac{\partial^2 U_i}{\partial x_j \partial x_l}\frac{\partial^2 U_i}{\partial x_k \partial x_l} + D_{\varepsilon^h} + S_l + S_{\varepsilon 4} \; . \tag{18}$$

The ε^h-equation is conventionally calibrated with constant coefficients $C_{\varepsilon 1}$, $C_{\varepsilon 2}$, $C_{\varepsilon 3}$ and a near-wall damping function f_ε. The length-scale limiter S_l and the pressure-gradient term $S_{\varepsilon 4}$ are additional source terms to sensitize the equation to effects of non-equilibrium turbulence.[15] To finally close the system of equations, the anisotropic dissipation rate tensor ε^h_{ij} is computed via an implicit relation:

$$\varepsilon^h_{ij} = f_s \overline{u_i u_j}\frac{\varepsilon^h}{k} + (1 - f_s)\,\frac{2}{3}\delta_{ij}\varepsilon^h \quad \text{with} \quad f_s = 1 - \sqrt{A}E^2 \; . \tag{19}$$

III. Test Cases

III.A. Computational Study of a Backward-Facing Step Flow

As a first study of the performance of the models described in II.B–II.D several TAU-computations of a backward-facing step (BFS) flow are performed. This is a standard test case for DES-based models, because it comprises a large region of massively separated flow. As a variety of experimental data is available for comparison, the test case of Driver and Seegmiller[11] is considered.

III.A.1. Numerical setup

Let us first define the computational domain: Based on a step height of $h = 0.0127$ m, a length of 4 h is prescribed before the step; behind the step the domain covers 25 h. The domain height is given by 8 h upstream, and 9 h downstream of the step, respectively. The spanwise extent is 4 h. Viscous-wall boundary conditions are chosen both at the top and the bottom of the domain. At the inflow a boundary-layer profile based on experimental data[11] is prescribed, while at the outflow all flow variables - except for the pressure which is held constant - are extrapolated from the interior. Periodicity is assigned in spanwise direction.
Three different grids are applied: While a 2D-plane of the coarse grid contains 6617 grid points, the number of points in the medium grid is twice that of the coarse grid both in x- and y-direction resulting in 25168 points. In spanwise direction, both grids contain 33 planes. The fine grid is obtained by again uniformly doubling the number of points both in x- and in y-direction (so an x-y-plane of the fine grid contains 101861 points) and applying 65 planes in spanwise direction. An x-y-plane of the coarse grid is shown in Fig. 1.
The Reynolds number based on the mean inflow velocity $U_\infty = 44.2$ m/s and the step height h is $Re_h = 37500$. The required physical time-step of $\Delta t = 1 \cdot 10^{-5}$ s is determined from the expected maximum velocity and the target grid spacing in the LES region of the fine grid according to Spalart.[17] This estimation is considered appropriate, as similar BFS computations did not show any considerable changes when the time step was further reduced.
Overall seven computations have been performed: While SA-DDES has been tested on all three grids, SA-IDDES computations have only been realised on the medium and the fine grid. The coarse grid was abandoned when it was found to suppress any 3D flow structures in the SA-DDES computation (see next section). For the analysis of mean results in the next section, all relevant flow variables from the unsteady computations are averaged in time over at least 10 convective time units, after an initial transient period of about 5 convective time units has passed. These mean variables are additionally averaged in homogenous spanwise direction, so that they can be regarded as statistically converged.
For comparison, 2D computations with the SA model and the ε^h-RSM have been performed on the medium grid, which is considered sufficiently fine for steady RANS computations.

III.A.2. Results

When analysing the computational results, both the effects of the underlying grids and the applied turbulence models are of interest. The presented figures are therefore grouped as follows: The upper picture in Fig.

2 and the left pictures in Figs. 3-5 show the results of all four models on the medium grid, allowing a comparison of different models on a single grid. The lower picture in Fig. 2 and the right pictures in Figs. 3-5 on the other hand illustrate the influence of the numerical discretization on the SA-DDES and SA-IDDES computations. The letters C, M, F in these pictures indicate results from the coarse, medium and fine grid, respectively (for better visibility the SA-IDDES results on the medium grid are not repeated).

First the prediction of the mean streamwise velocity U is considered at various x-coordinates along the flow domain. Fig. 2 shows all computational results in comparison with experimental data. According to the upper picture, both the SA-DDES and SA-IDDES results almost coincide and agree well with the experiment. The two RANS models perform less satisfactory, but there are notable differences in their results: While close to the step at $x/h = 1$ and $x/h = 2$ the ε^h-RSM compares quite well to the experiment and is superior to SA-RANS, it overpredicts the magnitude and size of the reverse flow farther downstream. This is caused by a too weak onset of turbulent Reynolds stresses in the front part of the separation, which delays reattachment and the subsequent recovery of the boundary layer.

The most striking observation in the lower picture of Fig. 2 is the much too large backflow region in the SA-DDES computation on the coarse grid, indicating a poor resolution of turbulent fluctuations in the LES region. On the fine grid both SA-DDES and SA-IDDES yield similar results and are superior to the SA-DDES computation on the medium grid (especially at $x/h = 4$). However, slight deviations from the measurements remain visible even in the fine-grid computations.

One of the most important criteria in BFS simulations is the correct prediction of the reattachment point which has been measured at $x/h = 6.38$ in the experiments. Figs. 3 and 4 show the skin-friction coefficient on the whole domain and in the region below the step, respectively. The two left figures indicate, that both the SA-DDES and the SA-IDDES computations on the medium grid yield similar results and agree well with the experiment. Reattachment is equally predicted at about $x/h = 5.9$, which is satisfactory. The SA-RANS model computes reattachment at $x/h = 6.6$, which is also a convincing result, although c_f is underestimated in other regions of the domain. While performing better than SA-RANS in the recovery region, the ε^h-RSM predicts reattachment too far downstream at $x/h = 7.6$ as already indicated by the velocity plots in Fig. 2. According to the right pictures, the flow computed with SA-DDES on the coarse grid does not reattach before $x/h = 12.8$ - this grid proves to be too coarse to resolve sufficient Reynolds stresses.

The second observation in the right pictures of Figs. 3 and 4 is rather surprising: The fine-grid computations with both SA-DDES and SA-IDDES show worse agreement with measurements than SA-DDES on the medium grid, as reattachment is shifted upstream to about $x/h = 5.2$ and slightly too high (negative) c_f-peak values are computed. Moreover, different from the medium-grid computations, SA-DDES and SA-IDDES show a clearly distinguishable behaviour on the fine grid.

The mean surface-pressure distribution on the step-wall shown in Fig. 5 enables further comparisons with the experiment. All computations, which accurately predict the reattachment location, also agree well with the measured c_p-minimum behind the step and the subsequent pressure rise in the separation region. However, regardless of the grid resolution (see Fig. 5, right), none of the models matches the pressure level behind reattachment. At least, all models apart from SA-RANS capture its slope quite well. In accordance with the c_f distribution, the ε^h-RSM shifts the pressure rise downstream and underpredicts the c_p-minimum.

Again, the SA-DDES results on the coarse grid in Fig. 5, right, deviate the most from the experiment and, in addition, reveal an incorrect pressure level at the inflow. Unlike all other computations, the specified pressure at the outflow does not yield the desired inflow conditions in this case, which is apparently due to the largely overpredicted separation size.

The last variable to look at is the instantaneous Q-criterion, which is an indicator for small-scale vortical structures in resolved turbulent flow. In Figs. 6-8 iso-surfaces of $Q = 200\ 1/\mathrm{s}^2$ for the three SA-DDES and two SA-IDDES computations are plotted.

The result of SA-DDES on the coarse grid, shown in Fig. 6, confirms that this grid is not able to resolve turbulence: Almost no 3D-structures can be seen and the resulting 2D-rolls are similar to the typical outcome of a 3D-URANS computation.[9] Fig. 7 shows the result of the SA-DDES (left) and SA-IDDES (right) computations on the medium grid. In both cases 3D structures can be observed, while the resolved scales seem to be slightly finer in the SA-DDES computation. As only a single value of Q at one fixed point in time is depicted, this observation should not be overrated. The computations on the fine grid with SA-DDES (left picture) and SA-IDDES (right picture) in Fig. 8 yield the most small-scale turbulent structures compared to the coarser meshes, while both models perform similarly on this grid.

Overall the results of the backward-facing-step computations can be summarized as follows: On sufficiently

fine grids, both SA-DDES and SA-IDDES yield very similar results and agree well with the experiment. By contrast, the ε^h-RSM overpredicts the reattachment length by about 20 % because of a too weak onset of Reynolds stresses around the separation core, while SA-RANS differs from measurements close behind the step and in the recovery region.
The coarse grid is found unsuited to resolve any significant turbulence with SA-DDES and therefore yields the largest deviations from the experiments, whereas the medium grid allows reasonable SA-DDES and SA-IDDES computations. As expected, simulations on the fine grid result in the greatest amount of turbulent small-scale structures. However, it is rather unclear why the medium-grid computations agree better with the measured c_f distribution and reattachment point than the results obtained on the fine grid.

III.B. Simulation of the HGR-01 Airfoil at Stall

The HGR-01 is a research airfoil designed to investigate the tail-plane stall at comparably low Reynolds numbers. Experiments took place in the low-speed wind tunnel MUB of the Institute of Fluid Mechanics, TU Braunschweig, at $Re = 0.65 \cdot 10^6$ using static pressure probes, oil visualization and particle image velocimetry (PIV).[13] Although the stall is of mixed type, i.e. a combination of laminar leading-edge separations and turbulent separations from the trailing edge, the experiments indicate that the flow is dominated by the trailing-edge separation up to angles of attack clearly beyond maximum lift ($\alpha = 16°$).

III.B.1. Numerical setup

In accordance with the experiments, the TAU-computations with SA-DDES and SA-IDDES are conducted at $Re = 0.65 \cdot 10^6$ and $Ma = 0.073$ and cover the stall process from almost fully attached flow at $\alpha = 12°$ up to lift breakdown induced by trailing edge separations at $\alpha = 16°$. The computational grid for the 3D computations is based on a 2D hybrid RANS grid obtained from a mesh convergence study.[13] To meet the requirements of a detached-eddy simulation it has been further refined in the expected separation region above the trailing-edge and the wake, yielding 650 x 112 points in the near-wall structured part of the x-z plane. This 2D grid, shown in Fig. 9, left, is uniformly extruded in spanwise direction with an extent of $L_z = 0.2c$ (see Fig. 9, right), and periodic boundary conditions are applied. Unless otherwise mentioned, a mesh with $n_z = 32$ spanwise layers is used in the simulations. In- and outflow is modelled via a farfield boundary condition in a distance of 100 chord lengths from the airfoil, thus neglecting the effects of wind-tunnel walls and installations throughout this study.
For each DES variant and grid, the simulations of the stall process begin with a restart based on a SA-RANS solution at $\alpha = 12°$, followed by further subsequent restarts while rotating the grid to reach higher angles of attack. The choice of the time step, $\Delta t = 1 \cdot 10^{-4}\ s$, (for $U_\infty = 25$ m/s and a chord length of $c = 1$ m in the computations) is again guided by Spalart.[17] The underlying SA-RANS model is activated at transition locations which were previously computed with TAU's e^N-based transition prediction module.[18] Corresponding to the experiment, transition to turbulence takes place in a small and stable laminar separation bubble near the nose which has very little effect on the trailing-edge separation. Where available, the results are compared to 2D-RANS computations with the Spalart-Allmaras model and the Low-Re ε^h-RSM.

III.B.2. Modification of the delay functions f_d and f_{dt}

Since large parts of the airfoil flow are expected to remain attached even at higher angles of attack, it is advisable to verify if the above-mentioned problems of modelled-stress depletion and grid-induced separations are actually cured. Recall that both DDES and IDDES apply "delay functions" (f_d and f_{dt}) to keep attached boundary layers safely in the RANS region. An appropriate test case is the flow at $\alpha = 12°$, as the trailing-edge separation computed with SA-RANS is so small here, that it is safe to expect the LES regions in SA-based DDES and IDDES computations to be limited to the wake region. Therefore, the results should be very similar to SA-RANS along the airfoil. However, as shown in Fig. 12, the Reynolds stresses in the boundary layer computed with SA-DDES are drastically reduced compared to SA-RANS, and the separation grows even far beyond the experimental results. Similar behaviour was found with SA-IDDES and for the grid with 64 spanwise layers, in fact suggesting the reappearance of grid-induced separations even with DDES and IDDES in this particular case.
To further study this behaviour, Fig. 10 shows velocity profiles U/U_∞, the eddy-viscosity ratio ν_t/ν and the DDES delay function f_d near the trailing edge on the upper surface. As discussed in Sec. II.B, f_d should

take a value of zero in the attached boundary layer to "shield" it from premature switching to LES mode. Instead, only about 50 % of the strongly decelerated boundary layer is covered when evaluating f_d based on a steady state SA-RANS solution (Fig. 10, left), apparently not enough to retain the required eddy-viscosity level to preserve the velocity profile with SA-DDES (Fig. 10, middle). On the other hand, the grid in the outer boundary-layer region is too coarse to possibly compensate the lacking modelled Reynolds stresses by directly resolving turbulent fluctuations. Moreover, as f_d itself depends on the decreasing eddy viscosity, the shielded part of the boundary layer is further reduced in a self-amplifying process (see Fig. 10, middle), so that the separation keeps on growing even after considerable simulation time.[a]

As the suspected problem of modelled-stress depletion is known to be associated with the mesh resolution in the RANS region,[6] a grid study is performed for further investigation. Based on the grid shown in Fig. 9, a series of grids has been generated which are independently coarsened in streamwise, wall-normal and spanwise direction. The computations with SA-DDES are 2D, i.e. with just one cell in spanwise direction, which is sufficient to evaluate the effect of the cell size on f_d and the eddy viscosity after five convective time units ($t/\Delta t_{conv} = 5$) restarting from a steady-state SA-RANS solution.

While the variation of wall-normal and spanwise resolution has only little influence on the flow field (not shown here), Fig. 11 shows a significant effect of coarsening the grid in streamwise direction by a factor of 4: unlike the fine grid, this mesh is actually able to retain the level of modelled stresses in the boundary layer, so that the flow remains mostly attached and stable. However, according to Fig. 11, this is not caused by the delay function f_d, which initially (at $t/\Delta t_{conv} = 0$) agree well on both grids, but it is due to the somewhat larger length scale ratio $l_{\mathrm{DDES}}/l_{\mathrm{RANS}}$ in the outer boundary layer, where the LES subgrid-scale Δ in both DDES and IDDES is dominated by the streamwise grid spacing. As a result, the eddy-viscosity destruction in Eq. (1) is smaller than on the fine grid which is now sufficient to preserve its overall level.

These observations indicate that the delay functions f_d and f_{dt}, which have been calibrated for a flat-plate flow,[6] may fail their purpose in applications with strong boundary-layer thickening due to pressure gradients. However, since a grid intentionally made coarse enough to avoid modelled-stress depletion by itself would not meet the required accuracy in the adverse-pressure gradient flow, we rather consider an ad-hoc modification to safely apply DDES and IDDES in the HGR-01 case. It is found that raising the factor 8 to 16 in f_d and f_{dt} is necessary to shield enough of the boundary layer to obtain a solution close to SA-RANS at $\alpha = 12°$ (see Fig. 10, right, and SA-DDES$_{16}$ in Fig. 12). The applicability of these new variants, which are called SA-DDES$_{16}$ and SA-IDDES$_{16}$ from now on, has been confirmed for higher angles of attack. That said, a more general approach directly including the effects of pressure gradients without affecting equilibrium boundary layers is certainly desirable.

III.B.3. Simulation of the stall process

To analyse the computational results at initial stall conditions, $\alpha = 12°$, time-averaged streamlines, as well as Reynolds shear stress and velocity profiles are compared to PIV measurements in Fig. 12 and 13. As expected, the modified variants SA-DDES$_{16}$ and SA-IDDES$_{16}$ now almost yield the same results as SA-RANS apart from the decreased Reynolds stresses in the wake. However, this implies that all three models share the SA-model's deficiency to correctly capture the effect of the adverse-pressure gradient along the airfoil, as the velocity and Reynolds-stress profiles in the trailing-edge region at $x/c = 0.7$ and $x/c = 0.95$ (see Fig. 13) strongly deviate from the experiments. The momentum loss and, as a consequence, the thickening of the boundary layer are underestimated, so that its tendency to separation is clearly reduced. These findings are confirmed by c_p- and c_f-plots along the airfoil in Fig. 14 and 15 which show that the SA-based computations yield too strong pressure recovery and high skin friction levels towards the trailing edge. Moreover, despite the decrease of modelled Reynolds stresses in the wake, no resolved turbulence is found as spanwise velocity components remain neglectable in the whole flow domain.

As also visible in Figs. 12 - 15, the ε^h-RSM with its terms S_l and $S_{\varepsilon 4}$ to account for non-equilibrium effects yields much better results than the SA model. Although the streamlines also indicate a slightly too small separation, the velocity profiles agree very well with the measurement apart from the near-wall backflow region at $x/c = 0.95$. The same goes for the computed turbulent shear stresses and the c_p distribution, which quite accurately follows the reduced pressure recovery at the trailing edge.

Raising the angle of attack to $\alpha = 14°$, the separation points computed with the SA-based models move upstream to about $x/c = 0.8$, as indicated by the c_f plot in Fig. 17. However, the backflow regions visible

[a]Note that Fig. 10, middle, just shows the initial stage of the growing trailing-edge separation.

in Fig. 16 remain very thin compared to the ε^h-RSM computation, which again agrees much better with the measured c_p distribution in Fig. 17. According to the skin friction in Fig. 17, the flow separation predicted with the ε^h-RSM covers almost 40 % of the airfoil's rear, i.e. twice as much as in the SA-based DES computations. Because of this mild separation, the DES models still do not resolve any turbulent fluctuations, and the results remain very close to RANS.
In order to obtain flow separations possibly large enough to generate turbulent content, α is further increased up to 16° which, according to the experimental lift curve in Fig. 20, is already far beyond maximum lift. While the ε^h-RSM only moderately overpredicts $c_{a,max}$ by about $\Delta c_a \approx 0.1$ and at $\Delta\alpha = 1°$ too high, the SA-RANS model does not even reach maximum lift $c_{a,max}$ before $\alpha = 16°$. At this point, both SA-DDES$_{16}$ and SA-IDDES$_{16}$ clearly deviate from SA-RANS and exhibit the lift drop common to airfoil stall.
Accordingly, the trailing-edge separations at $\alpha = 16°$ have grown to a considerable size, which is exemplarily shown for SA-IDDES$_{16}$ in Fig. 18. However, even with a separation starting at about 50 % chord length, the delay function f_{dt} in Fig. 18 still covers the whole backflow region and prevents the generation of resolved turbulence. Moreover, despite the rapid reduction of ν_t downstream of $x/c = 1.1$, even the wake is still virtually free of 3D structures suggesting a very slow onset of resolved turbulence in the LES region. This is illustrated by iso-surfaces of the Q-criterion in Fig. 19, showing only 2D vortical structures while the wake flow exhibits just minor spanwise oscillations with $|W/U_\infty| < 0.001$.
To study probable grid effects on the amplification of disturbances in the wake, another study is performed which comprises SA-DDES$_{16}$ computations on different meshes with increased spanwise resolution n_z and extent L_z. However, neither doubling the spanwise resolution to $n_z = 64$, nor increasing the domain span from $L_z = 0.2c$ up to $0.8c$ significantly increases the amplification of spanwise disturbances. The only influence is found for the grid with $n_z = 64$ and $L_z = 0.2c$, as the higher spanwise resolution apparently leads to a slight reduction of modelled stresses in the attached boundary layer so that the separation point moves a bit upstream (see Fig. 21).

III.B.4. Initial forcing of turbulent content

In a further attempt to generate turbulent content in the separated flow, an artificial forcing of LES mode in the trailing-edge region is introduced (similar to a zonal RANS/LES approach) which is supposed to be removed after turbulence has developed. Because of their formulation in terms of local flow variables, DDES and IDDES are assumed to show some dependency on the initial conditions which may help to retain resolved turbulence even after switching back to the original models. In particular, starting from the approximate separation point at about $x/c = 0.5$, the delay function in SA-IDDES$_{16}$ is set to $f_{dt} = 1$ which is found to be sufficient to obtain LES mode in the trailing-edge region apart from very near the wall. The approach is tested for $\alpha = 16°$ on the grid with $n_z = 64$, applying a reduced time step of $\Delta t = 5 \cdot 10^{-5}\ s$.
According to the snapshot of the computation with LES-mode forcing in Fig. 22, left, the eddy viscosity indeed rapidly decays in the LES branch, and the streamlines projected to the x-y plane exhibit a larger separation (compared to Fig. 18) with multiple vortex cores indicating resolved turbulent flow. This is confirmed by the visualization of the Q-criterion in the left of Fig. 23, showing small-scale 3D vortical structures in the separated flow region which, on the other hand, do not evolve before about $x/c = 0.65$, i.e. 15 % chord length behind the switch to LES mode. This proves that both the grid and the numerical method are capable of resolving turbulence, although its onset is still clearly delayed.
However, after switching back to the original SA-IDDES$_{16}$ and about 4 convective time units of further computation, the eddy viscosity shown in Fig. 22, right, has built up again, reducing the separated region back to the size and regular structure already known from Fig. 18. Accordingly, the trailing-edge region is again mostly free from turbulent eddies with only some remaining 3D structures being convected downstream (see Fig. 23, right).

IV. Conclusion

Two recently published variants of the detached-eddy simulation, the Delayed DES (DDES) and the Improved Delayed DES (IDDES), were applied to a backward-facing step flow and an airfoil at stall, and compared to RANS results of the Low-Re ε^h-Reynolds-stress model.
For the backward-facing step flow with massive, geometry-induced separation, a grid study with three different meshes is conducted. Apart from the coarse grid, which is not able to resolve any 3D turbulence,

SA-DDES and SA-IDDES yield equally good agreement with measured skin friction and velocity. Although the fine grid resolves more small-scale turbulent structures in the separated region, the mean-flow predictions are overall comparable to the medium-grid computations. However, full grid convergence could not be achieved. Both DES models show their advantages over RANS approaches for this kind of flow, as the ε^h-RSM is found to overpredict the separation size.
The simulations of the HGR-01 airfoil flow at stall, which is characterized by pressure-induced separations gradually growing from the trailing edge, reveal a number of issues associated with the present DES models. Both DDES and IDDES are still found to exhibit grid-induced separations due to modelled-stress depletion in this case which, however, can be cured with an ad-hoc modification of the model functions. Moreover, the DES simulations share the weak response of the underlying SA-RANS model to adverse-pressure gradients leading to underestimated trailing-edge separations regardless of the actual DES model applied. In contrast, the Low-Re ε^h-RSM captures the airfoil stall in good agreement with measurements, and is therefore considered a promising candidate for a future combination with DES.
Even with considerable separation size at high angles of attack, the sensor functions in both SA-DDES and SA-IDDES retain RANS mode throughout the whole separated region and prevent the generation of resolved turbulence. Attempts to enhance the amplification of disturbances by applying grids with increased spanwise extent and resolution as well as artificially introducing resolved turbulence at the beginning of the computation yield no significant improvement. Future applications of DES-based methods on airfoil stall therefore require RANS/LES sensors which are more sensitive to moderate separations as well as measures to amplify the generation of resolved turbulence in the LES branch.

Acknowledgments

The authors gratefully acknowledge the support of the "Deutsche Forschungsgemeinschaft" (DFG) which funded this research.

References

[1]Wilcox, D.C., *Turbulence Modelling for CFD*, Second edition, DCW Industries, La Canada, 1998.

[2]Pope, S., *Turbulent Flows*, Cambridge University Press, reprint, 2007.

[3]Spalart, P.R., Jou, W.-H., Strelets, M., Allmaras, S.R., *Comments on the Feasibility of LES for Wings, and on a Hybrid RANS/LES Approach*, Advances in DNS/LES, 1st AFOSR Int. Conf. on DNS/LES, Greyden Press, Columbus Oh., 1997.

[4]Deck, S., *Zonal detached-eddy simulation of the flow around a high-lift configuration with deployed slat and flap*, AIAA Journal, Vol. 43, pp. 2372-2384, 2005.

[5]Spalart, P. R.., Allmaras, S. R. *A one-equation turbulence model for aerodynamic flows*, La Recherche Aeorospatiale 1, 5-21, 1994.

[6]Spalart, P.R., Deck, S., Shur, M.L., Squires, K.D., Strelets, M., Travin, A., *A new version of detached-eddy simulation, resistant to ambiguous grid densities*, Theoretical and Computational Fluid Dynamics, Vol. 20, No. 3, pp. 181-195, 2006.

[7]Piomelli, U., Balaras, E., *Wall-layer models for large-eddy simulations*, Ann. Rev. Fluid Mech. 34, 349-374, 2002.

[8]Shur, M.L., Spalart, P. R., Strelets, M. and Travin, A., *A hybrid RANS-LES approach with delayed-DES and wall-modelled LES capabilities*, International Journal of Heat and Fluid Flow, Vol. 29, No. 6, pp. 1638-1649, December 2008.

[9]Spalart, P. R.. *Detached-Eddy Simulation*, Annual Review of Fluid Mechanics, Vol. 41, pp. 181–202, 2009.

[10]Mockett, C., Greschner, B., Knacke, T., Perrion, R., Yan, J., Thiele, F., *Demonstration of improved DES methods for generic and industrial applications*, in: Hasse, W., Peng, S.-H. (Eds.), Proceedings of Second Symposium on Hybrid RANS-LES Methods, Corfu, Greece, 17-18 June 2007.

[11]Driver, D.M. And Seegmiller, H. L., *Features of a Reattaching Turbulent Shear Layer in Divergent Channel Flow*, AIAA Journal, Vol. 23, No. 2, pp. 163-171, 1985.

[12]Kroll, N., Rossow, C.-C., Schwamborn, D., *The MEGAFLOW-Project - Numerical Flow Simulation for Aircraft*, Progress in Industrial Mathematics at ECMI 2004, Springer, Berlin Heidelberg New York, 2005.

[13]Wokoeck R., Krimmelbein N., Radespiel R., Ciobaca V., Krumbein A., *Simulation and Experiments of the Stall Behaviour of an Airfoil with Laminar Separation Bubbles*, AIAA-2006-0244, 2006.

[14]Jakirlić S., Hanjalić K., *A new approach to modelling near-wall turbulence energy and stress dissipation*, Journal of Fluid Mechanics, Vol. 459, pp. 139-166, 2002.

[15]Probst, A., Radespiel, R. *Implementation and Extension of a Near-Wall Reynolds-Stress Model for Application to Aerodynamic Flows on Unstructured Meshes*, AIAA-2008-770, 2008.

[16]Gibson, M.M., Launder, B.E., *Ground Effects on Pressure Fluctuations in the Atmospheric Boundary Layer*, J. Fluid Mech., Vol. 86., pp. 491-511, 1978.

[17]Spalart, P.R., *Young person's guide to detached-eddy simulation grids*, NASA CR-2001-211032, 2001.

[18]Krimmelbein, N., Radespiel, R., *Transition prediction for three-dimensional flows using parallel computation*, Computers & Fluids, Vol. 38, No. 1, pp. 121-136, January 2009.

V. Figures

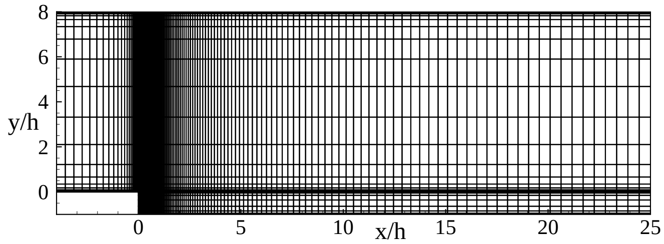

Figure 1. Sketch of an x-y plane of the coarse grid used in the backward-facing step (BFS) computation.

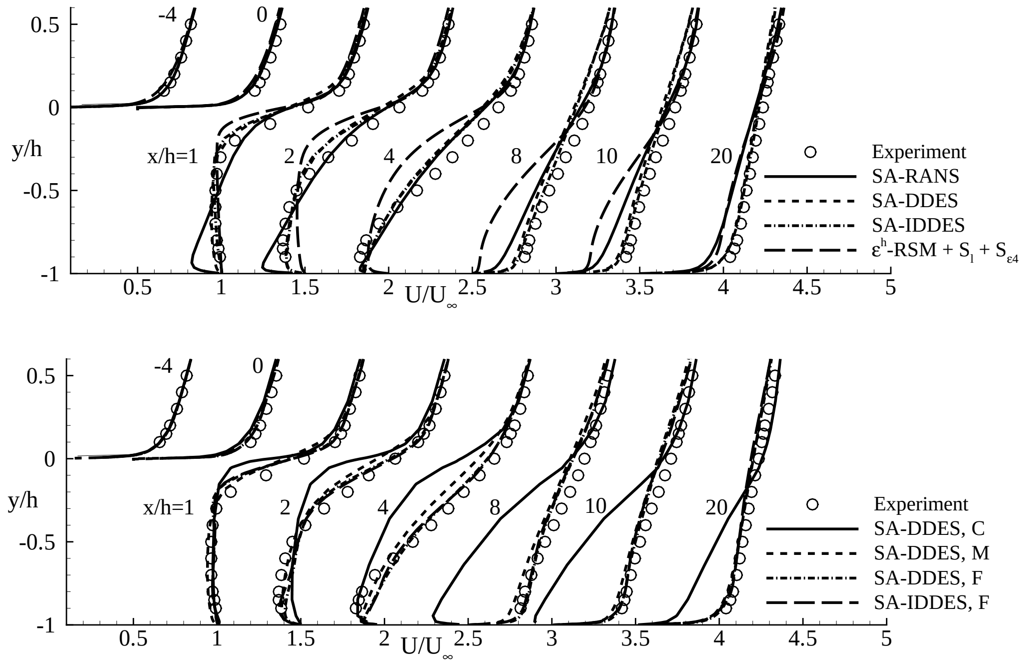

Figure 2. Mean velocity profiles of all BFS computations at various x-coordinates and comparison with experimental data. The results shown in the upper picture are based on computations on the medium grid. The letters C, M, F in the lower picture indicate computations on the coarse, medium and fine grid, respectively.

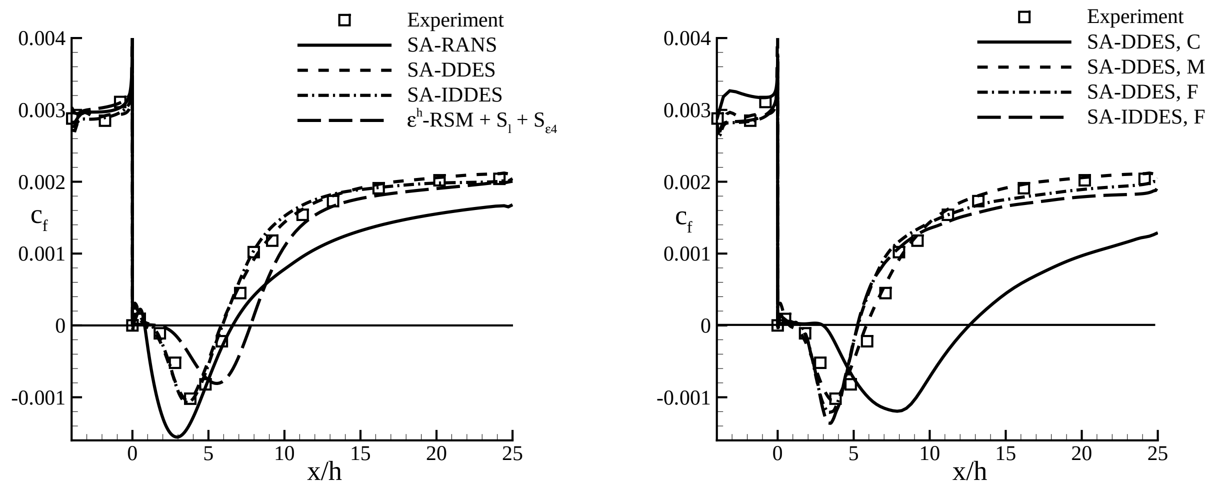

Figure 3. Mean skin-friction coefficients of all BFS computations and comparison with experimental data. The results shown in the left picture are based on computations on the medium grid. The letters C, M, F in the right picture indicate computations on the coarse, medium and fine grid, respectively.

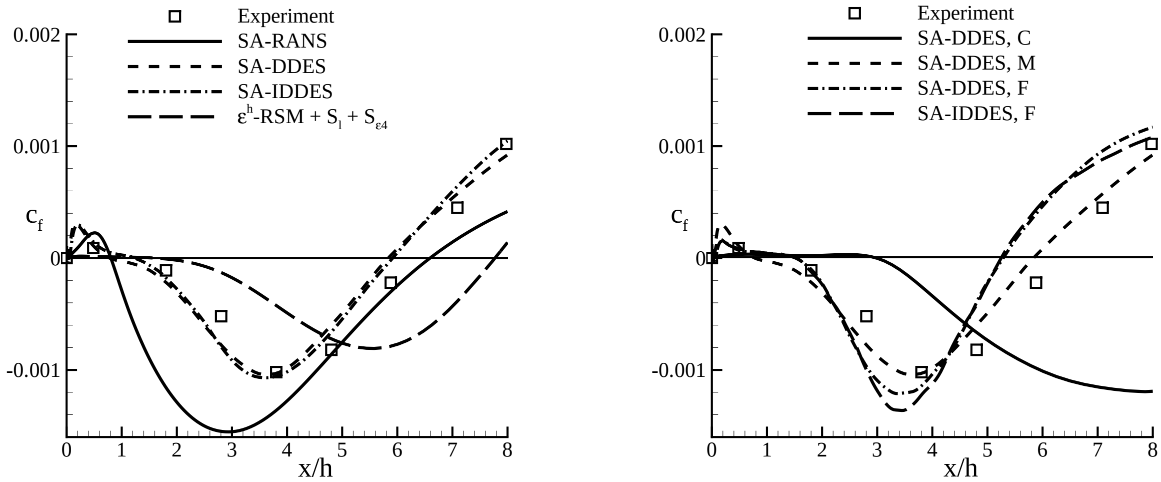

Figure 4. Mean skin-friction coefficients of all BFS computations and comparison with experimental data with focus on the separation region. The results shown in the left picture are based on computations on the medium grid. The letters C, M, F in the right picture indicate computations on the coarse, medium and fine grid, respectively.

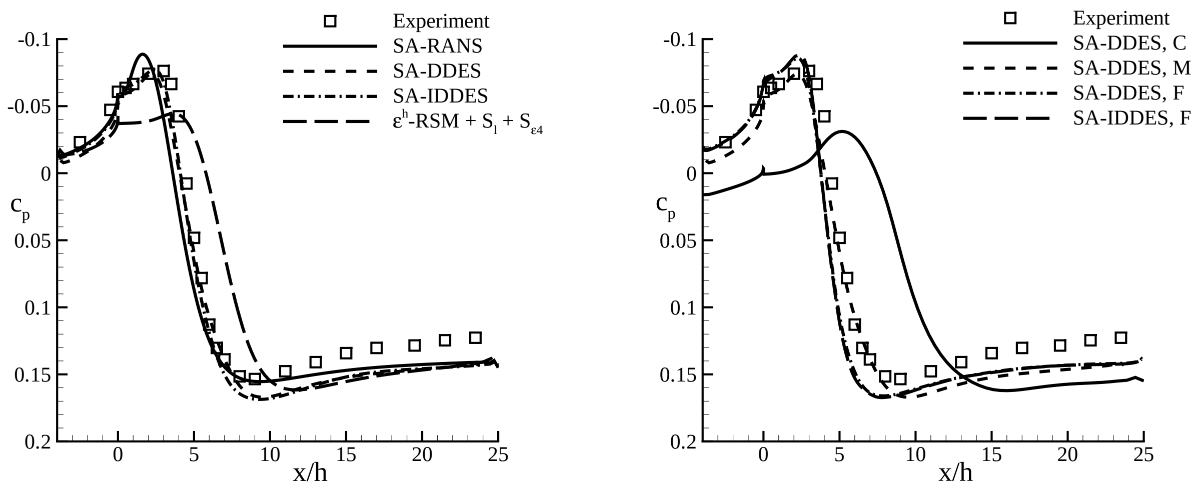

Figure 5. Mean surface-pressure coefficients of all BFS computations and comparison with experimental data. The results shown in the left picture are based on computations on the medium grid. The letters C, M, F in the right picture indicate computations on the coarse, medium and fine grid, respectively.

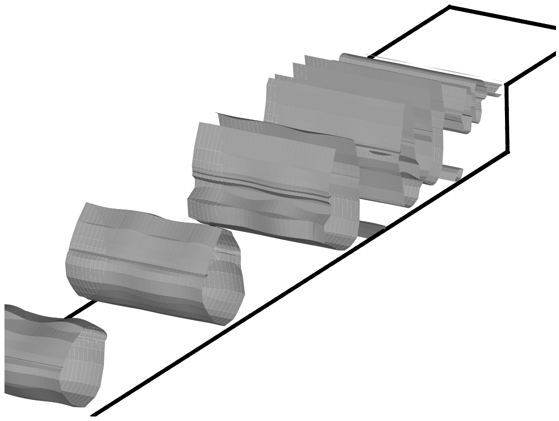

Figure 6. Iso-surfaces of the instantaneous Q-criterion at a value of $Q = 200\ 1/\mathrm{s}^2$. Shown is the result of the SA-DDES computation on the coarse grid.

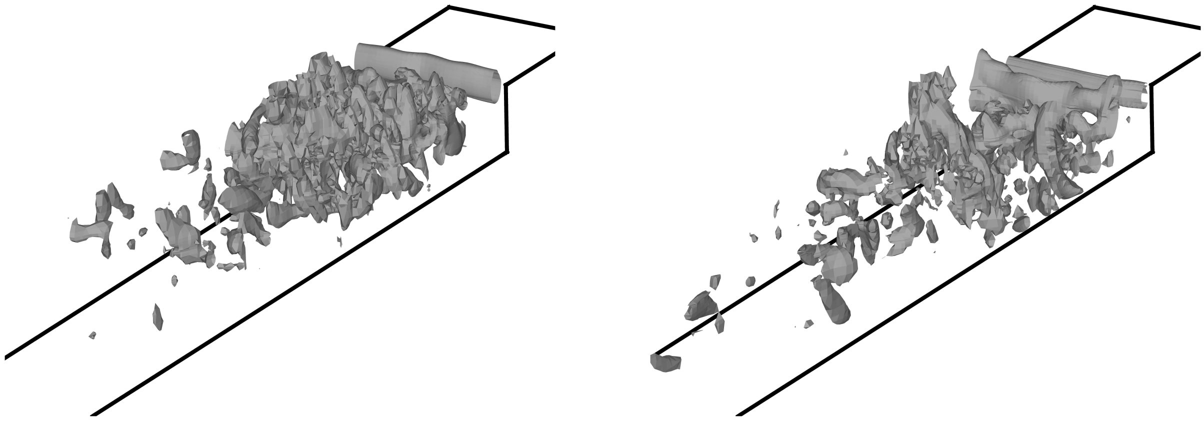

Figure 7. Iso-surfaces of the instantaneous Q-criterion at a value of $Q = 200\ 1/\mathrm{s}^2$. Shown are the results of the SA-DDES (left picture) and SA-IDDES (right picture) computations on the medium grid.

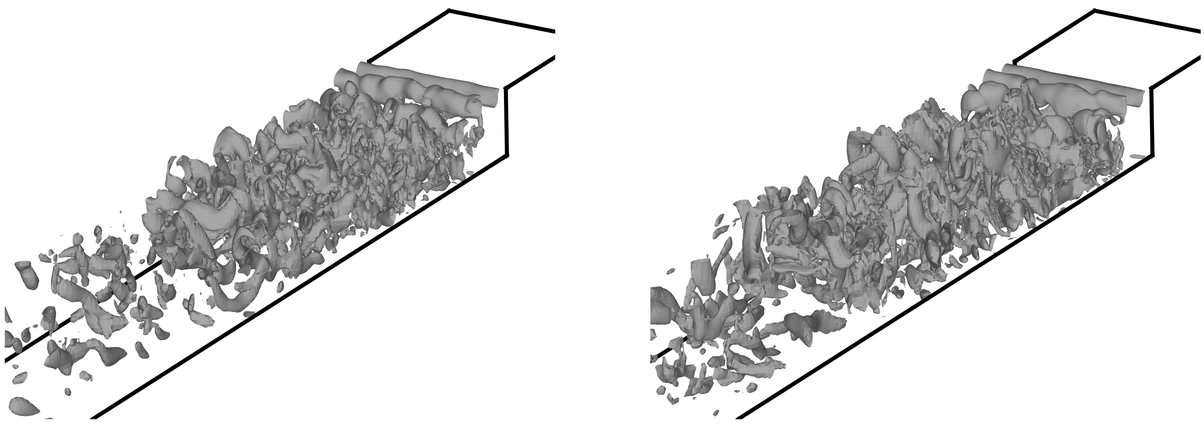

Figure 8. Iso-surfaces of the instantaneous Q-criterion at a value of $Q = 200\ 1/\mathrm{s}^2$. Shown are the results of the SA-DDES (left picture) and SA-IDDES (right picture) computations on the fine grid.

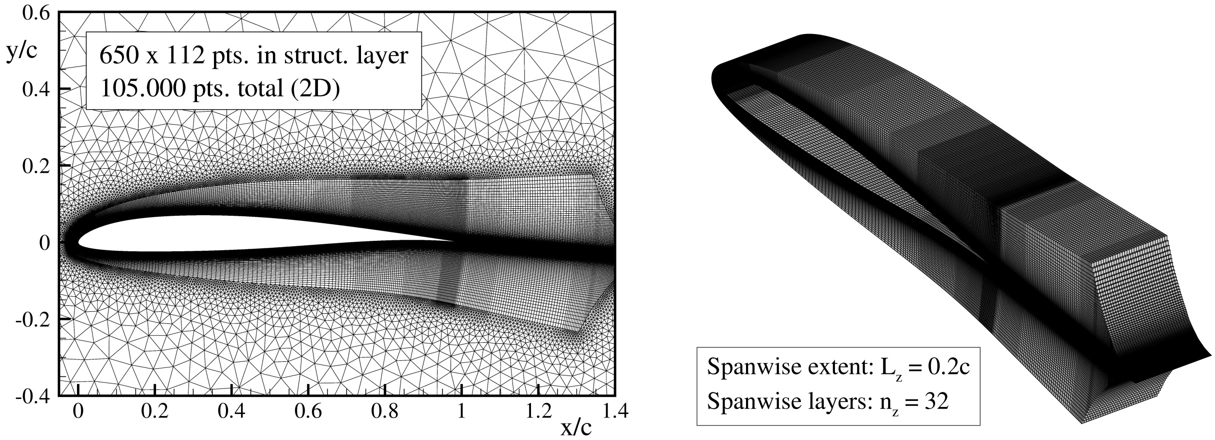

Figure 9. 2D hybrid c-type mesh (left) and structured part of the 3D mesh (right) for the HGR-01 airfoil.

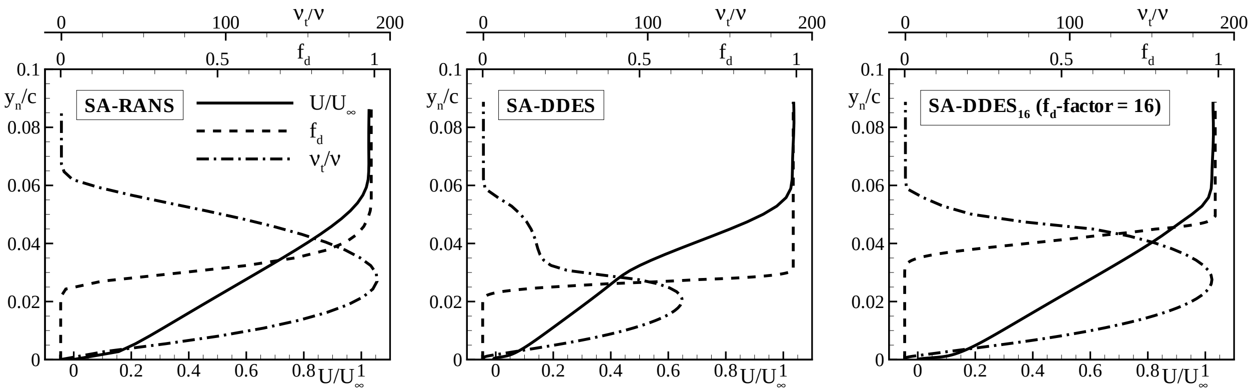

Figure 10. Profiles of streamwise velocity, delay function f_d and eddy viscosity at $x/c = 0.9$ of the HGR-01 airfoil at $\alpha = 12°$ computed with SA-RANS (left), SA-DDES (middle) and modified $SA\text{-}DDES_{16}$ (right).

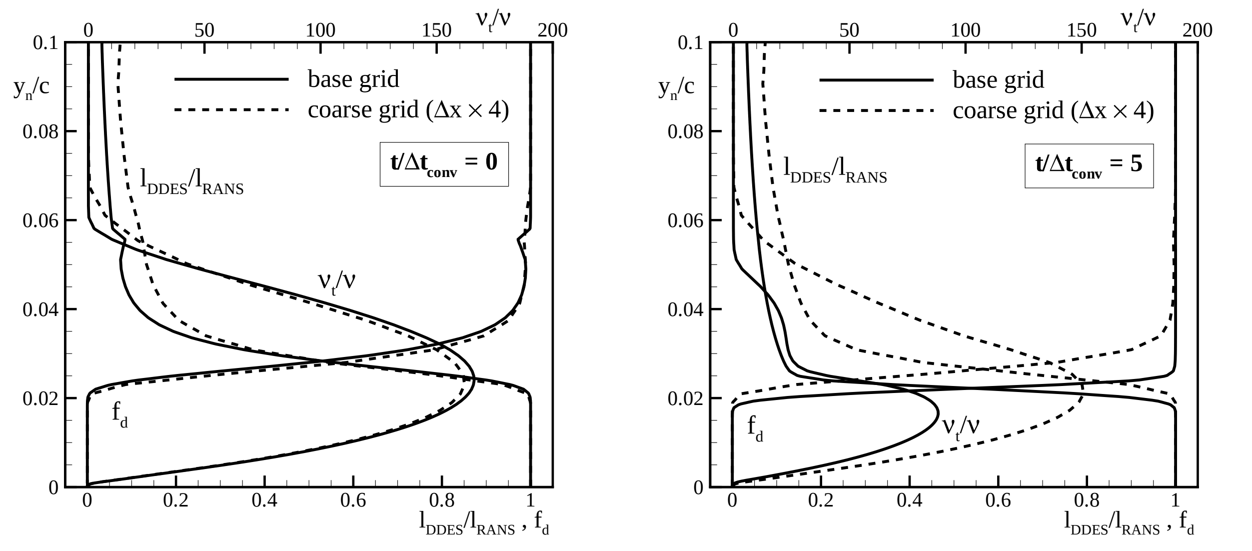

Figure 11. Influence of the streamwise grid spacing on the delay function f_d, the length-scale ratio l_{DDES}/l_{RANS} and the eddy viscosity at $x/c = 0.9$ of the HGR-01 airfoil $\alpha = 12°$. Results from SA-DDES at the start of the simulation (left) and after 5 convective time steps (right).

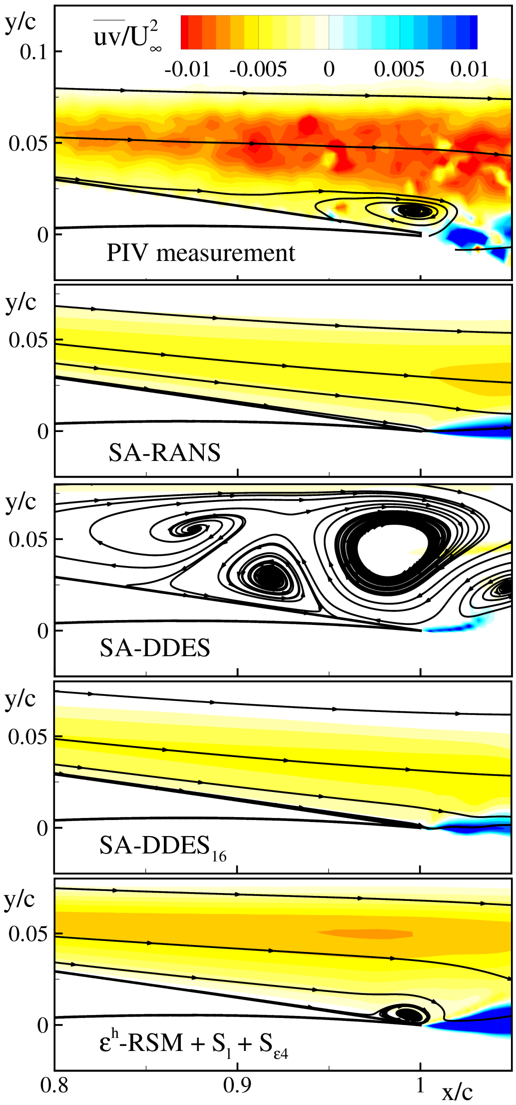

Figure 12. Streamlines and Reynolds shear stress at the trailing edge of the HGR-01 airfoil, $\alpha = 12°$.

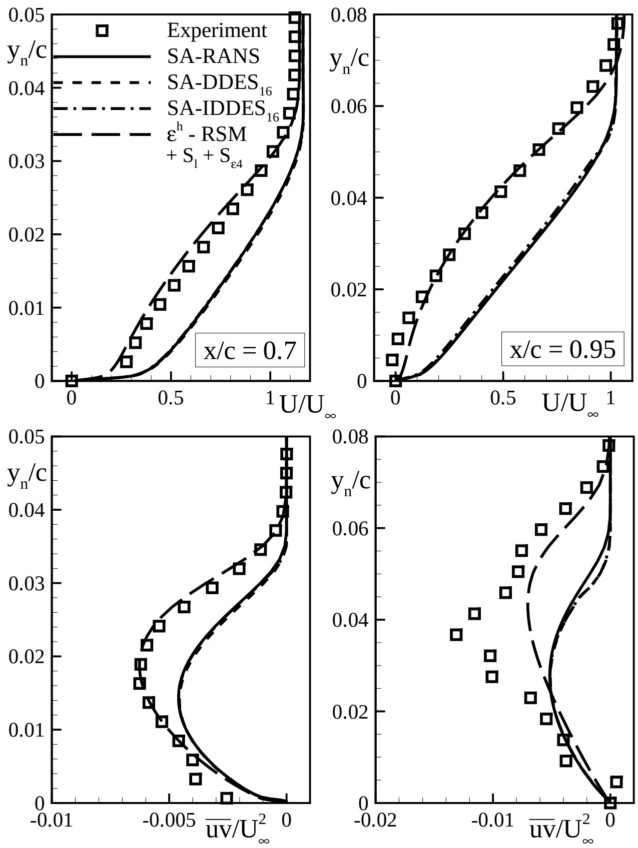

Figure 13. Mean velocity and Reynolds shear stress profiles at the trailing edge of the HGR-01 airfoil, $\alpha = 12°$.

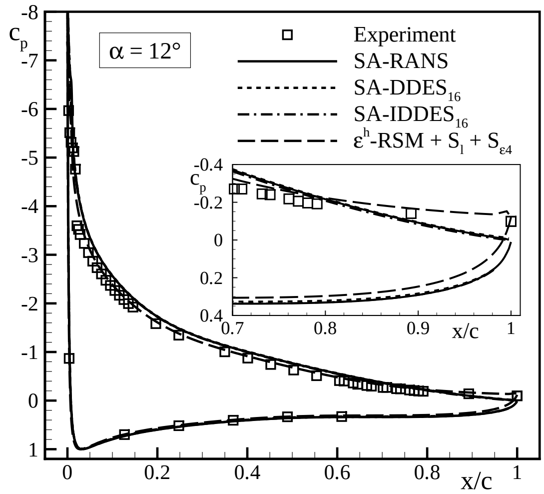

Figure 14. Mean surface-pressure distribution along the HGR-01 airfoil, $\alpha = 12°$.

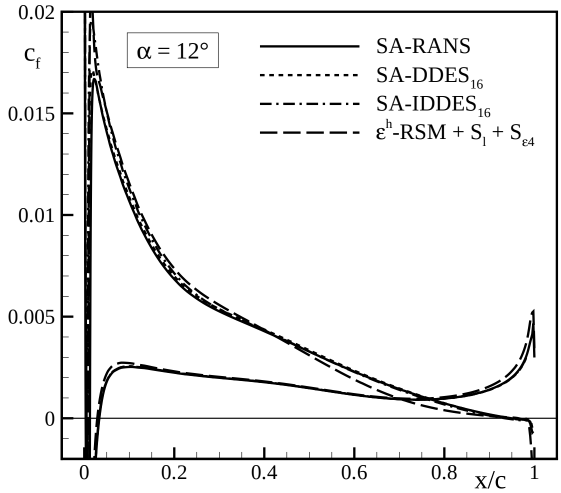

Figure 15. Mean skin-friction distribution along the HGR-01 airfoil, $\alpha = 12°$.

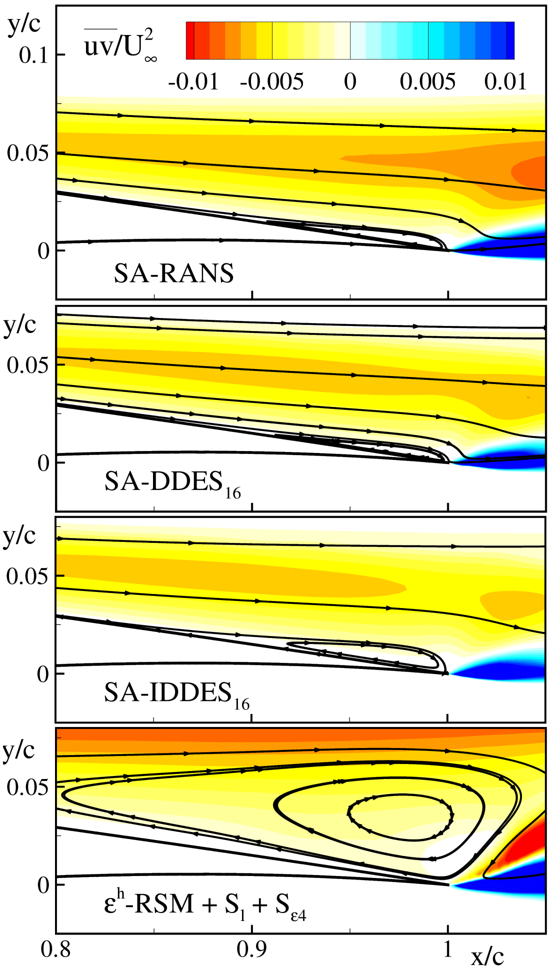

Figure 16. Streamlines and Reynolds shear stress at the trailing edge of the HGR-01 airfoil, $\alpha = 14°$.

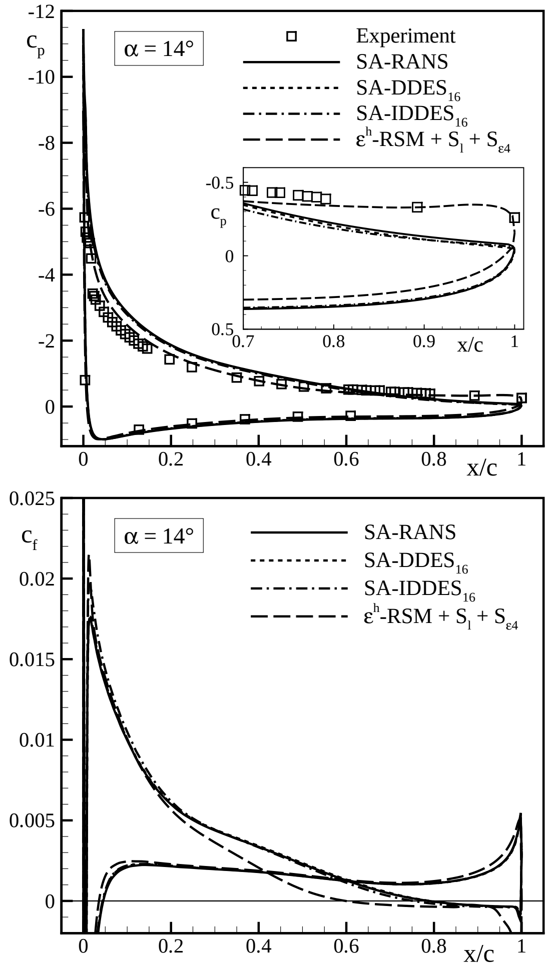

Figure 17. Mean surface pressure and skin-friction distribution along the HGR-01 airfoil, $\alpha = 14°$.

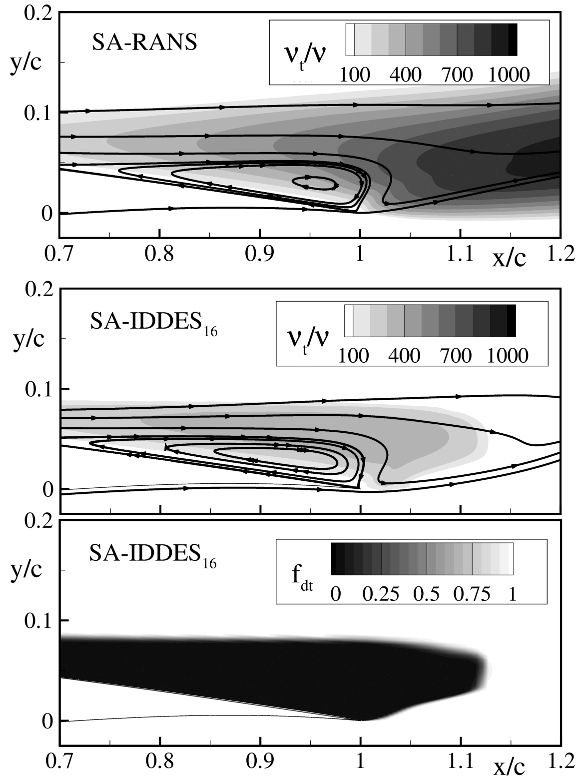

Figure 18. Streamlines, eddy viscosity and delay function f_{dt} from SA-IDDES$_{16}$ at the trailing edge of the HGR-01 airfoil, $\alpha = 16°$.

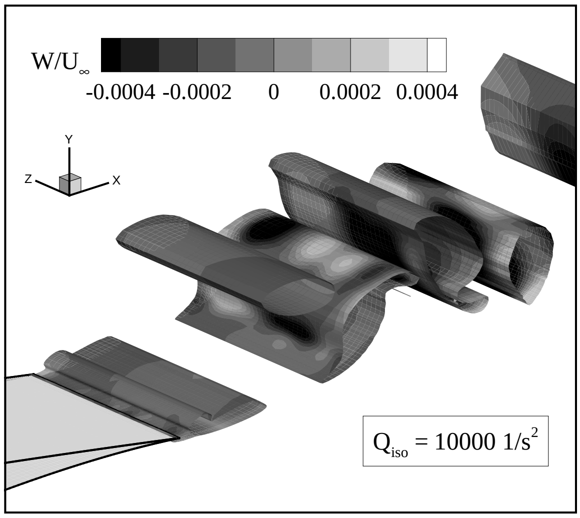

Figure 19. Iso-surface of Q-criterion coloured with instantaneous spanwise velocity at the trailing edge of the HGR-01 airfoil, $\alpha = 16°$, computed with SA-IDDES$_{16}$.

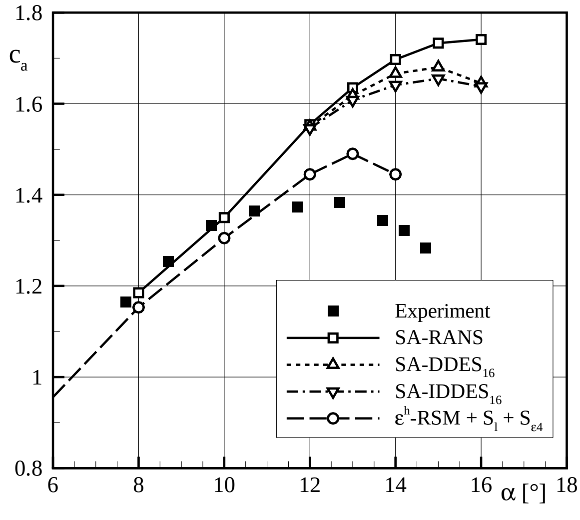

Figure 20. Computed and measured lift curve of the HGR-01 airfoil around stall.

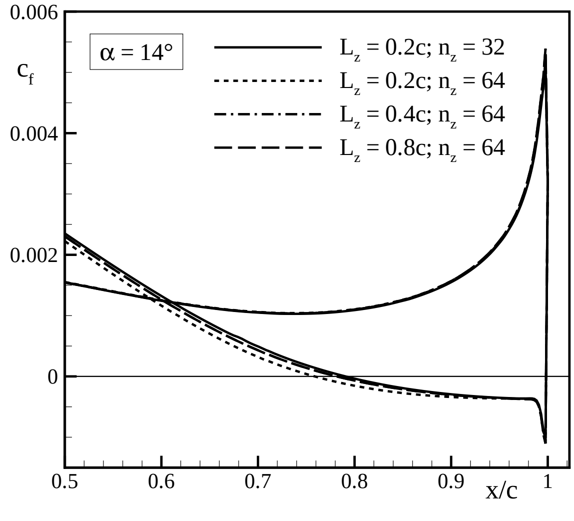

Figure 21. Influence of spanwise extent L_z and grid layers n_z on the mean skin friction of the HGR-01 at $\alpha = 14°$ computed with SA-DDES$_{16}$.

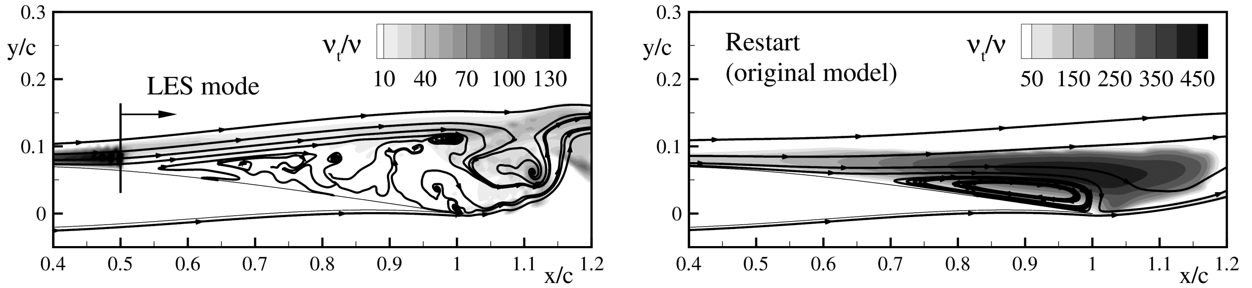

Figure 22. Projected instantaneous streamlines and eddy viscosity at the trailing edge of the HGR-01 airfoil, $\alpha = 16°$, with forced LES mode (left) and after switching back to original SA-IDDES$_{16}$ (right).

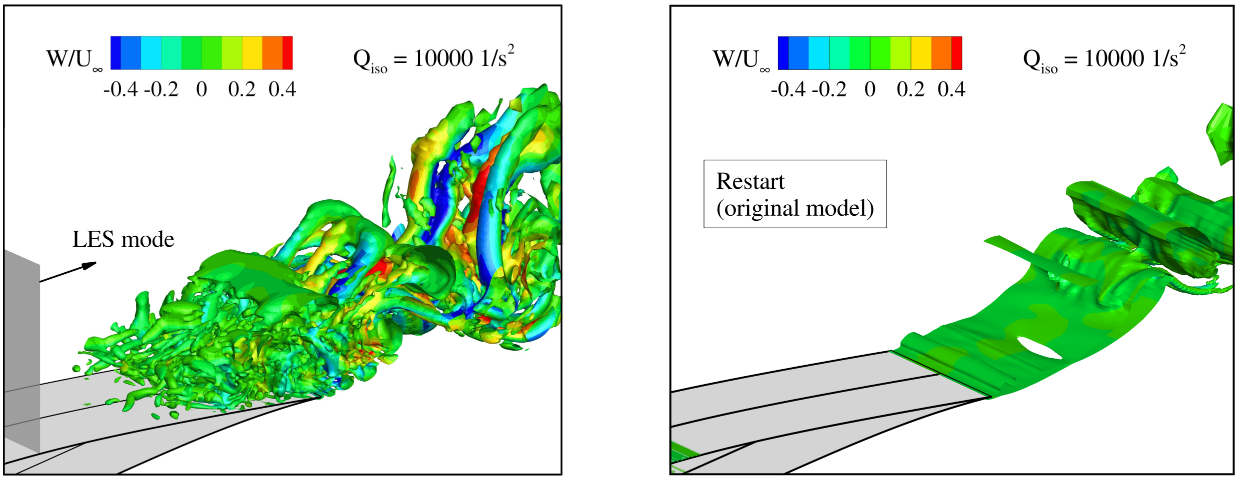

Figure 23. Iso-surface of Q-criterion coloured with instantaneous spanwise velocity at the trailing edge of the HGR-01 airfoil, $\alpha = 16°$, with forced LES mode (left) and after switching back to original SA-IDDES$_{16}$ (right).